Available online at www.sciencedirect.com
SCIENCE DIRECT®
Journal of Molecular Catalysis A: Chemical 226 (2005) 33–40
JOURNAL OF MOLECULAR CATALYSIS A: CHEMICAL
www.elsevier.com/locate/molcata

Effect of preparation parameters on $SrTiO_{3\pm\delta}$ catalyst for the flameless combustion of methane

Cesare Oliva[a,*], Lucia Bonoldi[b], Serena Cappelli[a], Laura Fabbrini[a], Ilenia Rossetti[a], Lucio Forni[a]

[a] *Dipartimento di Chimica Fisica ed Elettrochimica, Università degli Studi di Milano, via Golgi 19, I-20133 Milano, Italy*
[b] *Polimeri Europa, Novara, Italy*

Received 4 June 2004; received in revised form 20 September 2004; accepted 20 September 2004
Available online 27 October 2004

Abstract

Three $SrTiO_{3\pm\delta}$ catalysts have been compared. One of them (T3) was prepared by the traditional sol–gel procedure, the other two through the flame hydrolysis (FH) technique, in the presence of either 1.5 mol excess of citric acid (sample T2) or 3 mol excess of tartaric acid (sample T1) as complexing agent in the precursor solution. All the catalysts possessed the perovskite-like structure, with some $SrCO_3$ as impurity. T1 was more crystalline than the other two samples and showed the most active as catalyst for the flameless combustion of methane. Isolated Ti^{3+} ions were found in T3 by EPR analysis, while different EPR features were noticed with T1 and T2 and attributed to Ti^{4+}/O_3^-. A high concentration of isolated Ti^{3+} ions was observed with T1, accompanied by Ti^{4+}/O_3^- and by other paramagnetic species, probably Ti^{4+}/O^- and Sr^{2+}/O^-, not observed with the other samples. This difference between the samples T1 and T2, likely connected with the different temperature attained during the FH preparation process with the two different complexing agents, can explain the higher oxidising activity of the T1 sample.

Keywords: $SrTiO_3$ oxidation catalysts; Flame Hydrolysis preparation technique; ESR; Oxygen-centred radicals

1. Introduction

Transition metal oxide mixtures with perovskite-like structure are well known materials very active for the catalytic flameless combustion (CFC) of methane. Traditionally they have been prepared from the corresponding oxides through several cycles of high-temperature (950–1100 °C) calcination and milling [1], leading to a thermally resistant material, but with a too low surface area (ca. 1 m^2/g), hence with low catalytic activity. On the other hand, a well-known sol–gel-citrate (SGC) procedure [2] allows to obtain higher surface area (ca. 40 m^2/g). However, the relatively low final calcination temperature (usually less than 700 °C) attained with this procedure leads to a thermally poorly resistant material.

Both these properties, thermal stability and high surface area, can be achieved by preparing the material in nano-size particles, calcined at very high temperature. An innovative preparation method of this kind has been recently proposed [3], based on flame-hydrolysis (FH) of an aqueous solution of the precursor salts. However, samples of the same composition, but prepared from different precursors, may present rather different catalytic behaviour, probably connected with some subtle structural difference. In the present work we investigate three catalysts. Two of them (T1 and T2) have been prepared by FH, but from different precursors solution, the third one (T3) was prepared by the SGC technique. The aim was to compare these three samples as catalysts for the CFC of methane and to investigate the influence of the different preparation parameters on their catalytic properties.

* Corresponding author.
E-mail address: cesare.oliva@unimi.it (C. Oliva).
URL: http://www.dcfe.unimi.it.

1381-1169/$ – see front matter © 2004 Elsevier B.V. All rights reserved.
doi:10.1016/j.molcata.2004.09.023

2. Experimental

2.1. Catalysts preparation

A detailed description of the FH apparatus can be found elsewhere [3]. Briefly, a H_2/O_2 flame is used, in which a clear precursors' solution is nebulised. The nano-size particles so formed are collected by means of a 10 kV electrostatic precipitator.

The temperature attained by the flame in the region of the particle formation, measured by means of a Thermovision 900 FLIR systems IR camera in the 2–5 μm wavelength range, resulted nearly 1600 °C, being by ca. 8% higher for T1 than for T2. The high temperature and low residence time of the reagents in the flame guarantees a relatively high surface area and a very high thermal stability of the material.

2.2. Preparation of the solutions for FH and SGC preparation

2.2.1. FH

Five cubic centimetre of titanium *iso*-propoxide (Aldrich) were dropped under vigorous stirring in 50 cm^3 of distilled water, to obtain a fresh titanium oxide ($TiO_2 \cdot nH_2O$) suspension. Three mole excess of tartaric acid (sample T1) or 1.5 mol excess of citric acid (sample T2) were added to the solution, in both cases together with ca. 1 vol.% of 30 wt.% aqueous H_2O_2 solution, so to obtain the complete dissolution of the solid through complexation. The solution so obtained was mixed with another solution containing the stoichiometric amount of strontium nitrate and tartaric acid (sample T1) or citric acid (sampleT2) in 0.5/1 organic acid/Sr molar ratio, dissolved in the minimum amount of water. The excess water was finally removed in rotavapor, till 100 cm^3 residual volume [4].

2.2.2. SGC

The same solution used for FH T2 sample has been employed also for the SGC sample (T3). The only difference was the removing of water to dryness in rotavapor, till the formation of the solid. The latter was calcined in flowing air, with increasing temperature by 0.5 °C/min up to 250 °C, then by 1 °C/min up to 950 °C, kept for 1 h.

2.3. Catalysts characterisation

BET specific surface area (BET_{SSA}) and porosity were determined by means of a Micromeritics ASAP 2010 instrument. XRD analysis was carried out by a Philips PW1820 powder diffractometer, using the Ni-filtered Cu Kα radiation (λ = 0.15418 nm). Shape and size of the particles were determined by means of a Cambridge Stereoscan 150 scanning electron microscope (SEM). X-band EPR spectra were collected by means of a Bruker Elexsys instrument, equipped with an ER4102ST standard rectangular cavity and with a cryostatic ancillary apparatus. The magnetic field intensity has been accurately tested by an ER035M Bruker Teslameter accessory and the microwave frequency has been measured by the HP 5340A frequency counter.

The Q-band measurements were performed with a Bruker ESP300 E spectrometer equipped with a Q-band bridge and an ER5106QT cavity. The instrumental parameters were: 1 mW of microwave power and 1 and 2 G modulation amplitude at 97 K and room temperature, respectively.

The g_{iso} value of a Mn^{2+} multiplet with $a_{iso}(Mn) = 76$ G observed in the sample spectra ($g_{iso} = 1.9981$) was determined in a X-band measurement and employed successively as an internal reference. The EPR spectra have been simulated by the Bruker SimFonia programme.

2.4. Catalytic activity tests for the CFC of methane

Activity tests for the CFC of methane have been carried out by means of a bench-scale continuous apparatus. The catalyst (0.2 g), pelletised and then ground and sieved to 60–100 mesh particles, was mixed with 1.3 g of quartz particles of the same size and loaded into a vertical down-flow tubular quartz reactor, 7 mm i.d. The catalyst was kept in the isothermal central part of the reactor by means of quartz wool flocks. The empty parts of the reactor, above and below the catalyst, were filled with quartz beads (10–20 mesh). Reactant gases flow rates were controlled by means of MKS mod. 1259 mass flow regulators. The reactor was heated by an electric furnace, regulated by an Eurotherm mod. 812 TRC. The outlet gas was analysed in line by means of an HP 5890A HWD gas chromatograph, equipped with Porapak Q and MS 5A columns. Before the reaction the catalyst was activated in situ in flowing air (20 cm^3/min), while increasing temperature by 10 °C/min up to 600 °C, kept for 1 h. The activity tests were carried out by feeding a gas mixture composed of 10 cm^3/min of 1.04% methane in helium and 10 cm^3/min of air, while increasing temperature by 2 °C/min from 250 up to 650 °C.

3. Results

3.1. Catalysts characterisation

BET_{SSA} was about 12 m^2/g for both T1 and T2 samples, and ca. 1 m^2/g for T3. XRD analysis (Fig. 1) showed crystalline $SrTiO_{3\pm\delta}$ perovskitic structure for all the samples, accompanied by some $SrCO_3$ (characteristic reflections of the latter at $2\theta = 25.17°$, 25.80°, 36.53°, 44.08° [5]), present in smaller amounts with T2 and T3 than with T1. Furthermore, T1 was more crystalline than T2 and T3. SEM analysis (Fig. 2) showed for any sample, independently of their BET_{SSA}, relatively uniform, nearly spherical particles, 40–100 nm in size, often clustered into larger agglomerates, up to 500 nm in size.

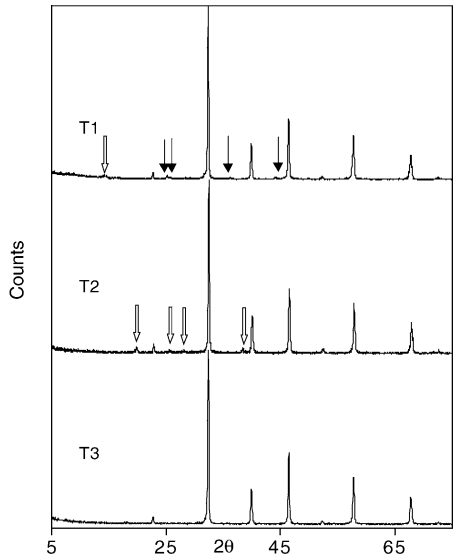

Fig. 1. XRD patterns. Black arrows: $SrCO_3$; white arrows: unidentified impurities. The patterns have been normalised, the original ordinate scale of T2 and T3 being 1/3 and 2/3, respectively, of that for T1.

3.1.1. EPR spectra of sample T1

The X-band EPR spectrum of sample T1 was composed of many features (see Fig. 3). A group of six weak and nearly equidistant lines of equal intensity, indicated by (*), belongs to some Mn^{2+} impurities. Other two lines A1, A2 appear at $g = 2.067$, 2.049, together with a broader feature A3 at $g = 2.021$ which contributes to a complex more intense absorption in the spectral region indicated by C. A feature B adds at higher field values. The last has been interpreted by computer simulation with $g_{//} \cong 1.982 < g_{\perp} \cong 1.983$, after recording it in detail and with several sample batches. Other four weaker lines, indicated with (+), add in this spectral region at ±9 and ±26 G from the B line. They have been re-examined by Q-band EPR spectroscopy (vide infra) where they appeared at the same distance from B. Also the A1, A2 and A3 lines have been investigated by Q-band EPR, but they were no more observable at 34 GHz (Fig. 4). On the contrary, the C band resolved at 97 K with Q-band EPR (Fig. 5), showing orthorhombic symmetry ($g_{xx} = 2.008$; $g_{yy} = 2.009$; $g_{zz} = 2.010$). A sample oxidation carried out in air at 600 °C for 1 h halved the intensity of the B line, with respect to the other lines of the EPR spectrum.

3.1.2. EPR spectra of sample T2

The X-band room temperature (RT) EPR spectrum of T2 shows a line absorption C′ around 3500 G much narrower than C observed with T1. However, also C′ is composed of more contributions. Indeed, an accurate simulation of X and Q-band signals reveals two contributions at $g = 2.011$ (A4) and at $g = 2.008$. The comparison between the RT and the 97 K Q-band tracks shows that at lower temperature A4 tends to saturate. Indeed, this line saturates also at RT with increasing microwave power (not shown). On the contrary, the feature with $g = 2.008$ resolves at 97 K into three components at $g = 2.008$, 2.009, 2.010 (Fig. 5), similarly to what reported for C with sample T1, but with spectral intensity by far lower than with the latter. Indeed, the track of T2 has been multiplied by a factor 3 in Fig. 3. Also the B line was present only as a faint trace in the spectrum of T2. In addition to the above signals, two hyperfine sextets ($a_{iso} = 76$ and 85 G, respectively) appear in the Q-band RT EPR of T2, due to Mn^{2+} impurities in two different sites, one of them being coincident with that observed with T1 (Fig. 4). Traces of Mn^{2+} ions were detectable also with X-band, but only after chemical reduction of the sample, suggesting that T2 was more oxidised than T1.

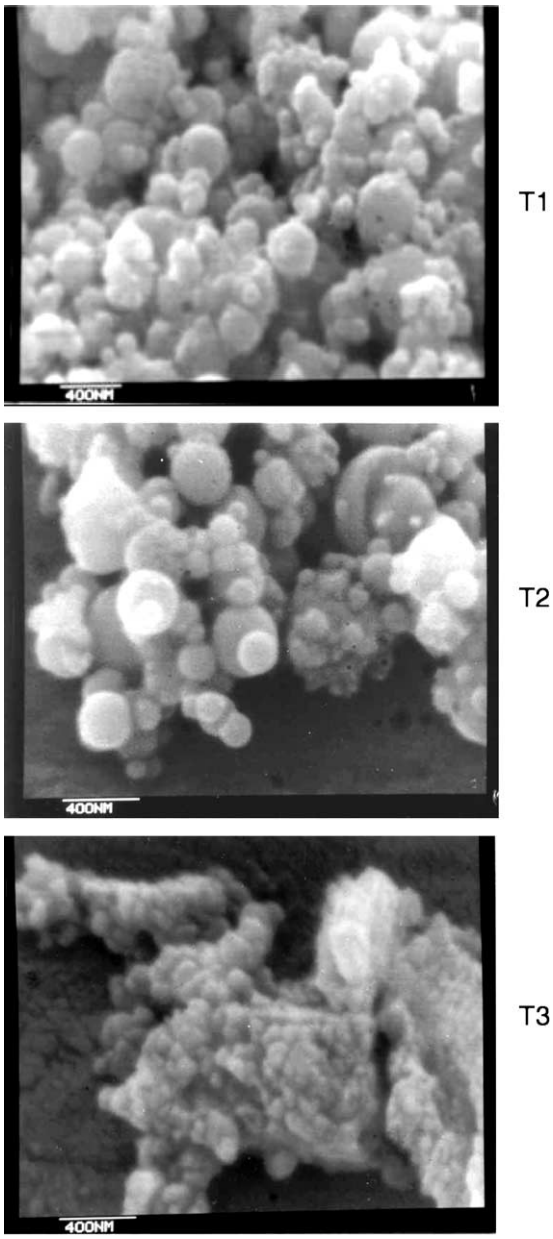

Fig. 2. Typical SEM images of the present samples.

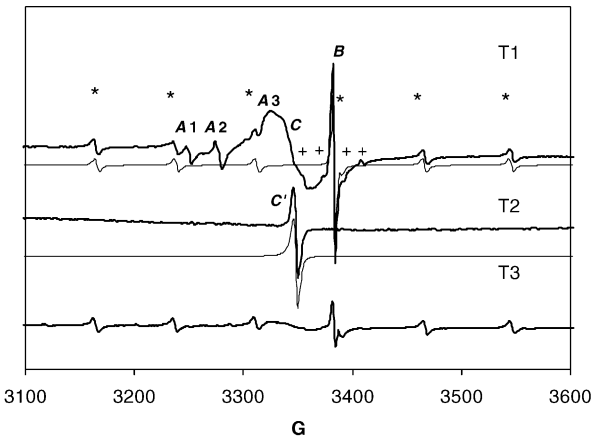

Fig. 3. EPR spectra at 296 K obtained with fresh samples (thick lines) and their simulation (thin lines, excluding the simulation of A3–C spectral region). The spectrum of sample T2 has been multiplied by a factor of 3. For the fitting parameters and the attribution of the lines, see text. (*) Mn^{2+} trace impurities.

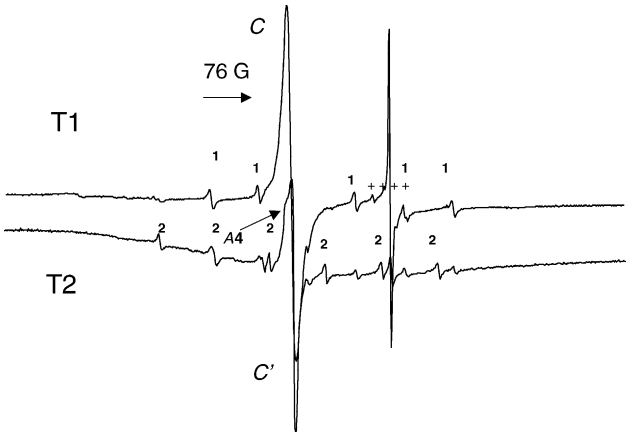

Fig. 4. Q-band EPR spectra of T1 and T2 at room temperature. 1 and 2 refer to the sextets of Mn^{2+} impurities in different sites.

3.1.3. EPR spectra of sample T3

Finally, the EPR spectrum of T3 showed the pattern due to Mn^{2+} and a low-intensity B line (Fig. 3), while traces of features similar to A3 and C became detectable at very high instrumental gains only.

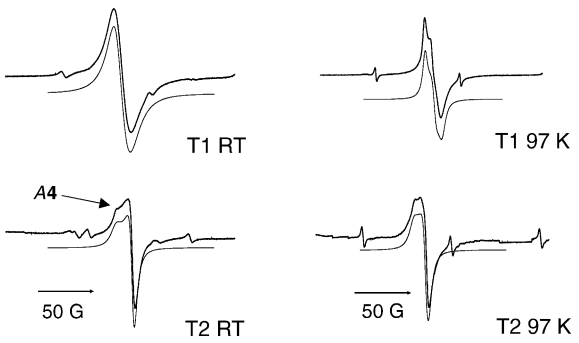

Fig. 5. Detail of C (T1 sample) and C′ (T2 sample) patterns in the Q-band EPR spectra at room temperature (RT) and at 97 K.

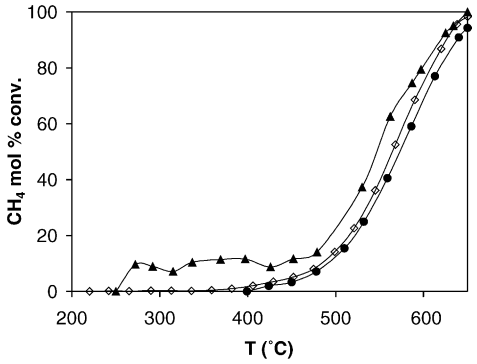

Fig. 6. Comparison of the activity of T1 (▲), T2 (◊) and T3 (●) catalysts for the CFC of methane.

3.1.4. EPR spectra after catalytic use

All these EPR patterns disappeared after the catalytic use of T1 and T2 for the CFC of methane, indicating that the corresponding paramagnetic species are involved in the catalytic reaction, i.e. that they are surface species. A new low-intensity, featureless spectrum remained only, preventing any reliable attribution to specific species. T3 behaved in part differently from T1 and T2. Indeed, the six Mn^{2+} lines were still observable, though with a reduced intensity, also after the catalytic use.

3.2. Activity tests for the CFC of methane

In-line analysis of the gas out coming from the methane CFC reactor was made every 10 min. The results are collected in Fig. 6 as mol% conversion of methane versus temperature. One may see that T1 was more active than T2 and T3. With T1 the reaction light off temperature (LOT) was 255 °C and the full conversion temperature (FCT) of the reactant was lower than 650 °C. Sample T2 showed LOT = 360 °C and FCT ≅ 660 °C and T3 was even less active than T2.

4. Discussion

4.1. EPR analysis

4.1.1. The B feature

The EPR line B (Fig. 3), characterised by $S = 1/2$, $g_{//} < g_{\perp} < g_e = 2.002319$, can be attributed to Ti^{3+} paramagnetic ions, investigated since long time by EPR in zeolites, silicalites, titanosilicates and other systems [6–13]. Indeed, it has been calculated that the Ti^{3+} g values, though strongly dependent on the crystal field, are always lower than g_e, the only exception being, possibly, Ti^{3+} in either a tetragonally compressed tetrahedral or in a trigonally distorted octahedral symmetry (unpaired electron in the d_{Z}^{2} orbital, $g_{//} \approx g_e$). This assignment is supported also by the fact that the intensity of the B line reduces during the sample oxidation, presumably because of the oxidation of Ti^{3+} to Ti^{4+}. Usually Ti^{3+} ions present anisotropic EPR signals in solid state centres [9,11],

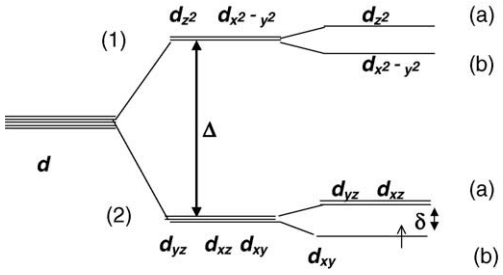

Fig. 7. $3d^1$ electron in a tetragonally elongated octahedral field. Double arrows indicate the tetrahedral splitting (△) and the further splitting (δ) due to tetragonal elongation. (a) and (b) levels exchange with each other in case of compression. (1) and (2) levels exchange with each other if the crystal field is tetrahedral instead of octahedral.

their g values strongly depending on the crystal field parameters. Both $g_{//} > g_{\perp}$ and $g_{//} < g_{\perp}$ cases have been observed [12] with different octahedrally co-ordinated Ti^{3+} complexes in frozen solution, in the presence of different crystal fields, and a nearly isotropic single EPR feature has been reported [7] with titanium-exchanged zeolites. In particular, values of g lower than g_e and $g_{//} < g_{\perp}$ can be obtained in a tetrahedral field with tetragonal elongation [14] or in a tetragonally distorted octahedral field [8,9,12–14]. Indeed, in the last case one has:

$$g_{//} \approx g_e - \frac{8\lambda}{\Delta}, \qquad g_{\perp} \approx g_e - \frac{2\lambda}{\delta} \tag{1}$$

where $\lambda = 154\,cm^{-1}$ is the spin–orbit coupling constant, and Δ and δ are the octahedral and tetragonal splitting parameters, respectively (Fig. 7): $g_{//} < g_{\perp}$ if $4\delta > \Delta$.

The experimental $g_{//} \cong 1.982 < g_{\perp} \cong 1.983$ values measured with line B fits this case with $\delta = 15958\,cm^{-1}$ and $\Delta = 60690\,cm^{-1}$. On the opposite, the formulae given for the tetrahedral tetragonally elongated case do not fit the present experimental g values, so that this possibility must be rejected. Furthermore, the assignment of the octahedral configuration to the titanium ion is in agreement with the expected symmetry for the B cation in the ABO_3 perovskitic structure.

At last, the four lines labelled by (+) in Figs. 3 and 4 can be attributed to Ti^{3+}–Ti^{3+} dimers in triplet configuration. Indeed, they appear equally spaced in X- and Q-band spectra (and consequently not at the same g values). Therefore, they are due either to electron spin/nuclear spin (hyperfine) or to electron spin/electron spin (fine) interaction. Excluding the hyperfine interaction on the base of their multiplicity and splitting, it is to be concluded that they result from a fine interaction. This multiplet is centred on the signal of the Ti^{3+} species ($g = 1.98$). Therefore, this triplet state can be attributed to a Ti^{3+}–Ti^{3+} dimer. In the approximation of pure dipole–dipole magnetic interaction, the half separation D_{dd} between the two outermost lines of the triplet spectrum ($26\,G \cong 24.0610^{-4}\,cm^{-1}$) allows to estimate the Ti^{3+}–Ti^{3+} distance $R = 10.2$ Å. This distance does not correspond to the distance between B sites in the perovskitic ABO_3 structure. This is not surprising, since only some titanium centres are reduced to the (III) oxidation state, while most of them keep their original (IV) oxidation state. No $\Delta m_s = \pm 2$ transition has been observed by us, as expected with such a small value of D_{dd}. Indeed, the intensity of such a feature decreases [15] as $(D_{dd}/g\beta B)^2$. For example, it has been reported [16] that this line appears with binuclear titanium(III) metallocenes only when the two Ti(III) ions, separated by $-O_2C(CH_2)_nCO_2-$ are not too far from each other, i.e. when $n \leq 6$. Furthermore, this feature was characterised by an intensity decreasing with increasing n and completely disappeared with $n = 8$ (i.e. with a Ti^{3+}–Ti^{3+} distance rather close to that above calculated by us), though the zero-field splitting was still measurable in the high-field part of the spectrum also in that case.

4.2. The A1–A4 and the C features

A1–A4 lines can be attributed to the perpendicular components of different M^+/O^- species, where M^+ is Sr^{2+} or Ti^{4+}. In fact, their g values are comparable to those attributed [17–25] to O^- adsorbed on metal oxides. In particular: $g_{\perp} = 2.071$, close to that of A1, has been reported for O^- on SrO [22], $g_{\perp} = 2.054$ has been measured [25] with O^-/Li^+ and $g_{\perp}$ values ranging between 2.016 and 2.045 have been measured for O^- adsorbed on Ti^{4+} centres [19–21,23], not too far from the values here reported for A2–A4. Also the disappearance of these lines from the Q-band spectra confirms their attribution. Indeed, it has been reported [18,25] that, for adsorbed O^- species, the $g_{\perp}$ feature strongly broadens in Q-band with respect to X-band spectra, so that it can be no more detectable with the former. This is due to the fact that the $g_{\perp}$ values of O^- are strongly dependent on the crystal field, being

$$g_{\perp} = g_e + \frac{2\lambda}{\Delta E} \tag{2}$$

in axial symmetry [17], where [18] $\lambda = 0.014$ eV is the spin–orbit coupling parameter, ΔE is the splitting between the two degenerate energy levels p_x^2, p_y^2 and the singly occupied p_z^1 (Fig. 8). Therefore, $\Delta E(1) = 0.2164$ eV, $\Delta E(2) = 0.300$ eV and $\Delta E(3) = 0.782$ eV can be calculated in correspondence of the three A1, A2 and A3 lines for O^- species adsorbed on a Sr^{2+} site and two different Ti^{4+} sites, respectively. Analogously, the signal A4, observed with T2 at $g = 2.011$, could be attributed to the $g_{\perp}$ component of the spectrum of a O^-/Ti^{4+} pair, with $\Delta E(T2) = 1.75$ eV. Theoretical calculations would lead to $g_{//}$ values close to g_e in these systems [17]. However, it has been reported [17] that this evaluation is not in agreement with the g values measured with O^- adsorbed on surfaces. Indeed, the spin–orbit coupling constant of the cation interacting with O^- and stabilizing it will also influence its $g_{//}$ value. As a consequence, $g_{//}$ values of O^- of 2.0013, 2.006 and even 2.012 have been observed [17] for O^-/Mg^{2+}, O^-/Mo^{6+} and O^-/W^{6+}, i.e. with the increasing spin–orbit coupling constant of Mg^{2+}, Mo^{5+} and W^{5+}, respectively. In our case, a spin–orbit coupling con-

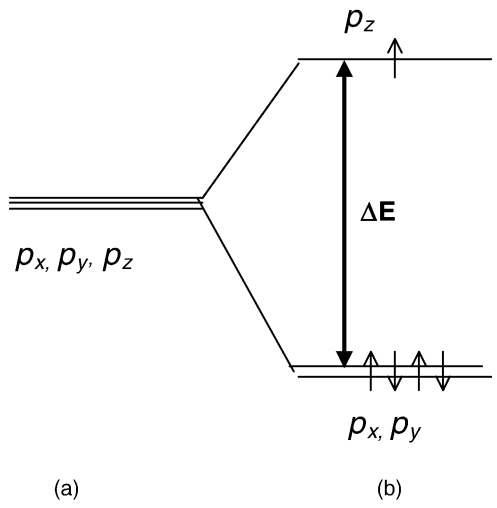

Fig. 8. Energy level diagram of the O^- ion: (a) free ion, (b) in an axial crystal field.

stant $\lambda \cong 154\,cm^{-1}$ can be attributed to O^-/Ti^{4+}, close to that of Ti^{3+}. Therefore, by interpolating the above reported literature values of $g_{//}$ as a function of λ, a $g_{//}$ value of O^- between 2.003 and 2.004 can be expected in the present case, contributing to the higher-field part of the C broad feature. Therefore, the fact that no EPR contribution is detectable for these species at $g_{//}$ values closer to g_e indicates that they are species interacting with a cation. However, also other paramagnetic species contribute to C. In particular, its g mean value $\langle g(C)\rangle = \langle g(C')\rangle = 2.009$, observed with T1 and T2 sample, respectively, is close to that reported [27–29] for O_3^-/Ti^{4+} in irradiated TiO_2, in which O_3^- can be thermally stable at temperatures up to 130 °C [30]. However, the present g tensor is less anisotropic than those reported for pure single-oxides [30], i.e. for relatively dense-packed systems, characterised by a rather low ion conductivity. In the present case, the O_3^- ions are located within perovskite-like mixed oxides, i.e. in a much more open structure, allowing higher ion mobility. This could explain the lower anisotropy observed by us along with the correct $\langle g\rangle$ value for the O_3^- species. Therefore, we have attributed the C′ line and the main contribution to C to adsorbed O_3^- species formed through the reaction [17]:

$$O^- + O_{2(g)} \leftrightarrow O_3^-$$

$$O_{3(g)}^- + \text{solid}^+ \rightarrow [O_{(3)}^- - \text{solid}^+]$$

Also O_2^-/Ti^{4+} could contribute [19–21] to the lower-field part of C, i.e. to the A3 feature. However, the stability of this line would be in contrast with this attribution. All these EPR data of oxygen-based species in T1 and T2 samples are collected in Table 1.

The difference between the $g_\perp$ ($\equiv g_{xx} = g_{yy}$) values of A1–A4 lines can be related to a different strength of the $M^+ - O^-$ ($M^+ = Ti^{4+}$ or Sr^{2+}) interaction. The splitting ΔE increases for adsorption at stronger surface crystal fields, as it occurs for example on higher charge cations, as Ti^{4+} with respect to Sr^{2+}, yielding lower $g_\perp$ values. The further decreasing values of $g_\perp$ (Table 1) for T1 and T2 catalysts shows that at least three different sites would be occupied by O^- radicals with T1, whilst only one site, different from the previous three, would be present in T2. By contrast, O^- radicals should not form, or should be present only as traces, in T3. The elementary steps involved in the formation of these ions could be [17,26]:

Table 1
EPR data of oxygen-based species in T1 and T2 samples

Sample	Line	Species	g_{xx}	g_{yy}	g_{zz}
T1	A1	O^-/Sr^{2+}	2.067	2.067	≥2.003
	A2	O^-/Ti^{4+}	2.049	2.049	≥2.003
	A3	O^-/Ti^{4+}	2.021	2.021	≥2.003
	C	O_3^-/Ti^{4+}	2.008	2.009	2.010
T2	A4	O^-/Ti^{4+}	2.011	2.011	≥2.003
	C	O_3^-/Ti^{4+}	2.008	2.009	2.010

$$\text{solid} \rightarrow \text{solid}^+ + e^-$$

$$O_{2(g)} + 2e^- \rightarrow 2O^-$$

$$O^- + O_{2(g)} \leftrightarrow O_3^-$$

$$O^- + \text{solid}^+ \rightarrow [O^- - \text{solid}^+]$$

where $solid^+$ is either Sr^{2+} or Ti^{4+} and the activation of oxygen through the first two (thermodynamically unfavoured) reactions occurs through its adsorption and incorporation into the oxide crystal lattice. Indeed, the experimental results show that the FH preparation technique yields the formation of electron-rich activated oxygen species, likely during the high temperature treatment employed when atmospheric molecular oxygen could react with the electron-rich activated oxide surface [17,25,26].

4.3. Catalytic activity

Sample T3 showed a lower catalytic activity than the other two samples. This could be attributed to its lower BET_{SSA}. However, T1 and T2, though possessing nearly the same BET_{SSA}, are characterised by a different catalytic activity (Fig. 6). Then, this must be attributed to the presence of different species on their surface. Indeed, the main difference between T1 and T2 samples is that O^-/Ti^{4+} is present essentially in the former only, while O_3^-/Ti^{4+} has been observed with both of them. On the other hand, T1 is more active as catalyst, in particular at $T <$ ca. 400 °C (Fig. 6). Therefore, the presence of O^- species seems crucial for the catalytic activity of the sample, in particular at lower temperature. Indeed, it is well known that both O^- and O_3^- are reactive towards alkanes [31,32] and alkenes [29,33,34]

and that O^- is about 100 times more reactive than O_3^- [30,34].

The overall oxygen-species-involving mechanism could then be described as:

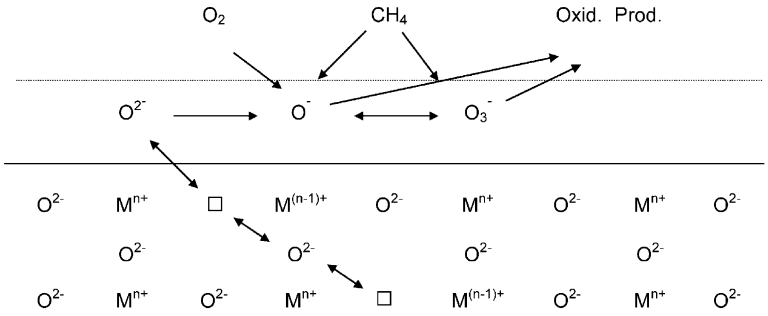

similarly to what reported by Bielanski and Haber [26]. In it the activation of the substrate (CH_4) could take place by dissociative chemisorption and further oxidative dehydrogenation, as reported [31] for the reaction of alkanes with surface O^- species.

O^- ions in different sites can contribute differently to the catalytic performance. In fact, the different interaction strength in the couple O^-/M^+ at each M^+ site influences the availability of oxygen species from the catalyst to the reacting substrate and the electronic orbitals energy levels of the reactive O^- species. Indeed, the higher electropositivity (i.e. lower charge, vide supra) of Sr^{2+} with respect to Ti^{4+}, confirmed by the higher $g_\perp$ values (Table 1 and Eq. (2)) should enhance the basicity of the O^- ion, so favouring the catalytic activity through an easier deprotonation of methane and hence its oxidation, as suggested [25] for the Li-doped MgO. Furthermore, the fact that in the catalytically worst of the three samples, i.e. in T3, only Ti^{3+} is present, confirms that this is not the main catalytic species. In addition, during reaction T1 re-oxidises better than T3. In fact, after catalytic use all the described EPR patterns disappear with T1 only, in which Mn^{2+} would oxidise to higher oxidation states. This could not be verified with T2, since in it the Mn ionic impurities were in a more oxidised state even before reaction.

The best catalysts proved T1 and T2, both prepared by the FH method and possessing a significant surface concentration of Ti^{4+}/O_3^-. In addition, a significant amount of Ti^{4+}/O^- is present in T1, which results the best catalyst. This difference between T1 and T2 can be attributed only to the difference in their preparation procedure, i.e. to the nature and concentration of the complexing agents in the precursor solution, leading to different temperatures during the FH process, the better catalyst (T1) being prepared at a flame temperature ca. 8% higher than T2.

5. Conclusions

The main conclusions one can draw from the present investigation are: (i) perovskite-like mixed oxide catalysts confirm once more to be a class of very versatile materials; (ii) their properties can be tailored in many ways, e.g. by changing preparation method, preparation conditions, nature and composition of precursor materials, final calcination temperature, etc., so to confer them specific catalytic properties; (iii)last, but not least, even apparently negligible differences in a given preparation procedure can afford important differences in physical–chemical characteristics and hence in catalytic properties of the finished material.

Acknowledgements

We are indebted with Dr. S. Marengo, Stazione Sperimentale per i Combustibili, S. Donato Milanese (Milano), for his help in measuring the flame temperature in the FH preparation method.

References

[1] M.S.G. Baythoun, F.R. Sale, J. Mater. Sci. 17 (1982) 2757.
[2] M.F.M. Zwinkels, S.G. Järås, T.A. Griffin, Catal. Rev. Sci. Eng. 35 (1993) 319.
[3] L. Forni, I. Rossetti, Appl. Catal. B: Environ. 38 (2002) 29.
[4] J. Garcia-Jaca, J.L. Pizarro, J.I.R. Larramendi, L. Lezama, M.I. Arriortua, T. Rojo, J. Mater. Chem. 5 (1995) 227.
[5] Selected Powder Diffraction Data, JCPDS, Swarthmore, PA, file 5-418 (1974–1982).
[6] Y. Ono, K. Suzuki, T. Keii, J. Phys. Chem. 78 (1974) 218.
[7] F. Khan, P. Yue, L. Rizzuti, V. Augugliaro, A. Brucato, Ind. Eng. Chem., Prod. Res. Dev. 22 (1983) 238.
[8] Tuel, J. Diab, P. Gelin, M. Dufaux, J.-F. Dutel, Y. Ben Taarit, J. Mol. Catal. 63 (1990) 95.
[9] M. Prakash, H. Mi Sung-Suh, L. Kevan, J. Phys. Chem. B 102 (1998) 857.
[10] G. Li, X. Wang, X. Guo, S. Liu, Q. Zhao, X. Bao, L. Lin, Mater. Chem. Phys. 71 (2001) 195.
[11] K. Chaudhari, R. Bal, D. Srinivas, A.J. Chandwadkar, S. Sivasanker, Micropor. Mesopor. Mater. 50 (2001) 209.
[12] S. Van Doorslaer, J.J. Shane, S. Stoll, A. Schweiger, M. Kranenburg, R.J. Meier, J. Organometall. Chem. 634 (2001) 185.
[13] Y.M. Kim, P.J. Bray, J. Chem. Phys. 53 (1970) 716.
[14] J.E. Wertz, J.R. Bolton, Electron Spin Resonance. Elementary Theory and Practical Applications, McGraw-Hill, 1972, p. 317.
[15] N.M. Atherton, Electron Spin Resonance. Theory and Applications, Wiley, 1973, p. 232.
[16] L.C. Francesconi, D.R. Corbin, A.W. Clauss, D.N. Hendrickson, G.D. Stucky, Inorg. Chem. 20 (1981) 2059.
[17] M. Che, A.J. Tench, Adv. Catal. 31 (1982) 77.

[18] S. Schlick, L. Kevan, J. Phys. Chem. 81 (1977) 1093.
[19] C.A. Jenkins, D.M. Murphy, J. Phys. Chem. B 103 (1999) 1019.
[20] A.L. Attwood, J.L. Edwards, C.C. Rowlands, D.M. Murphy, J. Phys. Chem. A 107 (2003) 1779.
[21] A.L. Attwood, D.M. Murphy, J.L. Edwards, T.A. Egerton, R.W. Harrison, Res. Chem. Intermed. 29 (2003) 449.
[22] O.J. Rubio, H.T. Tohver, Y. Chen, M.M. Abraham, Phys. Rev. B 14 (1976) 5466.
[23] M. Shiotani, G. Moro, J. Freed, J. Chem. Phys. 74 (1981) 2616.
[24] M. Che, J.C. Mc Ateer, A.J. Tench, J. Chem. Soc., Faraday Trans. I 74 (1978) 2378.
[25] J.-X. Wang, J.H. Lunsford, J. Phys. Chem. 90 (1986) 5883.
[26] A. Bielanski, J. Haber, Oxygen in Catalysis, Dekker, New York, 1991, p. 150.
[27] P. Meriaudeau, J.C. Vedrine, J. Chem. Soc., Faraday Trans. II 72 (1976) 472.
[28] A.R. Gonzalez-Elipe, G. Munuera, J. Soria, J. Chem. Soc., Faraday Trans. I 75 (1979) 748.
[29] Y. Takita, M. Iwamoto, J. Lunsford, J. Phys. Chem. 84 (1980) 1710.
[30] M. Che, A.J. Tench, Adv. Catal. 32 (1983) 1.
[31] K. Aika, J. Lunsford, J. Phys. Chem. 81 (1977) 1393.
[32] Y. Takita, J. Lunsford, J. Phys. Chem. 83 (1979) 683.
[33] K. Aika, J. Lunsford, J. Phys. Chem. 82 (1978) 1794.
[34] M. Iwamoto, J.H. Lunsford, J. Phys. Chem. 84 (1980) 3079.